Supplementary information

Crystallographic, Optical, and Electronic Properties of the $Cs_2AgBi_{1-x}In_xBr_6$ Double Perovskite: Understanding the Fundamental Photovoltaic Efficiency Challenges

Laura Schade[1], Suhas Mahesh[1], George Volonakis[2], Marios Zacharias[3], Bernard Wenger[1], Felix Schmidt[4], Sameer Vajjala Kesava[1], Dharmalingam Prabhakaran [1], Mojtaba Abdi-Jalebi[5], Markus Lenz[4], Feliciano Giustino[6,7], Giulia Longo[8], Paolo G. Radaelli[1] and Henry J. Snaith[1]

[1] Clarendon Laboratory, Department of Physics, University of Oxford, Oxford OX1 3 PU, United Kingdom

[2] Univ Rennes, ENSCR, INSA Rennes, CNRS, ISCR (Institut des Sciences Chimiques de Rennes), UMR 6226, France

[3] Department of Mechanical and Materials Science Engineering, Cyprus University of Technology, P.O. Box 50329, 3603 Limassol, Cyprus

[4] University of Applied Sciences and Arts Northwestern Switzerland (FHNW), School of Life Sciences, Institute for Ecopreneurship, 4132 Muttenz, Switzerland

[5] Institute for Materials Discovery, University College London, Malet Place, London, WC1E 7JE, United Kingdom

[6] Cavendish Laboratory, Department of Physics, University of Cambridge, JJ Thomson Avenue, Cambridge CB3 0HE, United Kingdom

[7] Oden Institute for Computational Engineering and Sciences, The University of Texas at Austin, Austin, Texas 78712, USA

[8] Department of Physics, The University of Texas at Austin, Austin, Texas 78712, USA

[9] Department of Mathematics, Physics and Electrical Engineering, Northumbria University, Ellison place, Newcastle upon Tyne NE18ST, United Kingdom

1) Structural characterization

1.1 Single crystals

Single crystal X-ray diffraction has been performed using an Agilent Supernova Diffractometer with Mo-Kα radiation to investigate the structural properties of the material. We performed the symmetry analysis with the use of the Isotropy Suite [1]. In Figure S1, we show the results of the fittings for the $Cs_2AgIn_xBi_{1-x}Br_6$ single crystals. The F^2_{calc} parameters almost perfectly coincide with the F^2_{obs} ones, demonstrating the extremely high quality of the crystals. Table ST2 contains the structural information for the fittings. Table ST1 shows the values of indium percentages (in comparison with the bismuth content) determined from Inductively Coupled Plasma Mass Spectrometry (ICP-MS) and X-ray diffraction. The XRD values have been calculated from the site occupancy in the structural refinement. For ICP-MS measurements, crystals (5-15 mg) were dissolved fully in concentrated HBr including 30min sonication treatment. Samples were then appropriately diluted with milliQ water (18.2 MΩcm). Quantification was carried out using an external calibration from single-element standards (Sigma-Aldrich) prepared in milliQ water (18.2 MΩcm) from 0-50 µg/L, matrix-matched to the corresponding HBr amount. Analysis was carried out using an Agilent 8800 ICP-QQQ-MS system on $^{115}In^+$ and $^{209}Bi^+$ using helium as a collision gas (5 mL/min). $^{103}Rh^+$ was used as an internal standard to account for possible matrix effects. We decided to use the ICP-MS values as our final percentages throughout all the manuscript, as they are more precise.

Table ST1 Indium percentage in single crystals determined by ICP-MS and XRD, in comparison with the starting percentage of indium that has been added to the starting solution.

%In in solution	%In (ICP-MS)	%In (XRD)
0	0.00208 ± 0.00388	0
1	1.18 ± 0.03	1 ± 4
5	7.25 ± 0.38	1± 2
10	12.1 ± 0.3	10 ± 3
15	17.0 ± 0.9	12 ± 2
20	25.4 ± 0.4	21 ± 3
50	25.1 ± 0.3	23 ± 2

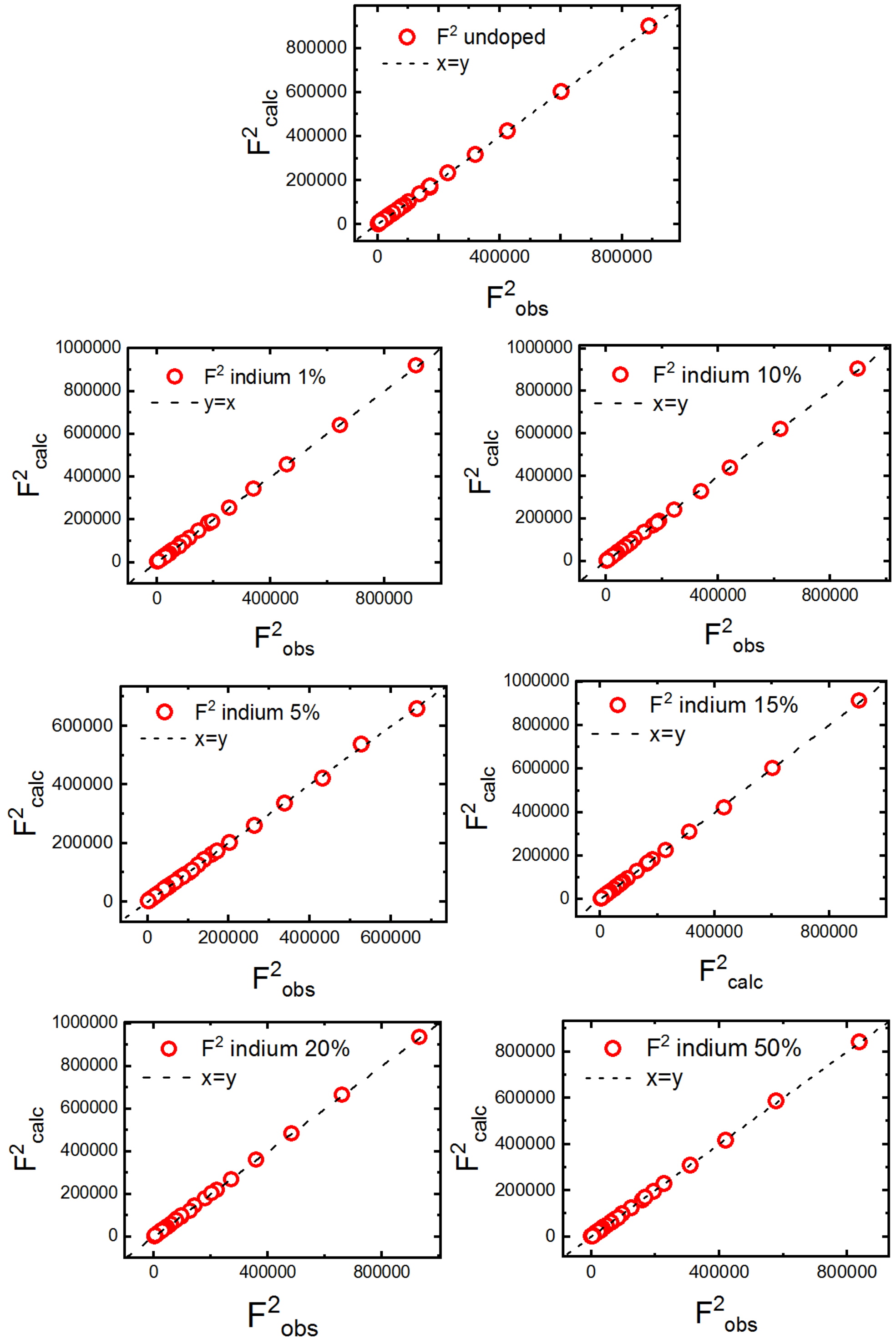

Figure S1 Plot of F^2_{calc} versus F^2_{obs} for the structural refinement of $Cs_2AgIn_xBi_{1-x}Br_6$ single crystals. The black line is a guide to the eye.

Table ST2 Lattice parameters and atomic coordinates from $Cs_2AgBi_{1-x}In_xBr_6$ single crystals fittings. Number in parentheses are statistical errors of the last significant digit. In $Fm\bar{3}m$, the atoms are located at the following Wyckoff positions Cs: 8c(1/4,1/4,1/4) , Bi/In: 4a(0,0,0) , Ag: 4b(1/2,1/2,1/2) , Br: 24e(x,0,0).

x	a (Å)	x(Br)	Occ(In)	R_{int}/R_w
0	11.2741(2)	0.25093(2)	-	5.33/5.07
1	11.26101(1)	0.2508(2)	0.01(4)	9.24/7.13
12	11.2375(3)	0.24988(2)	0.10(3)	7.25/5.82
17	11.2289(2)	0.24971(1)	0.12(2)	4.34/4.26
25	11.20772(1)	0.24885(1)	0.23(2)	4.62/4.54

1.2 Polycrystalline powders

Powder X-ray diffraction has been performed using a PANalytical X'Pert PRO Diffractometer with Cu-Kα radiation. Figure S2 shows the Rietveld refinements for all the samples. Structural parameters are reported in Table ST3. We notice the presence of impurity phases in the XRD patterns of PW10, PW35, PW45, and PW60, that we have not been able to characterize. The percentage of indium has been extrapolated using the occupancy of indium also in this case, and then compared with the ICP-MS results, as shown in Table ST4.

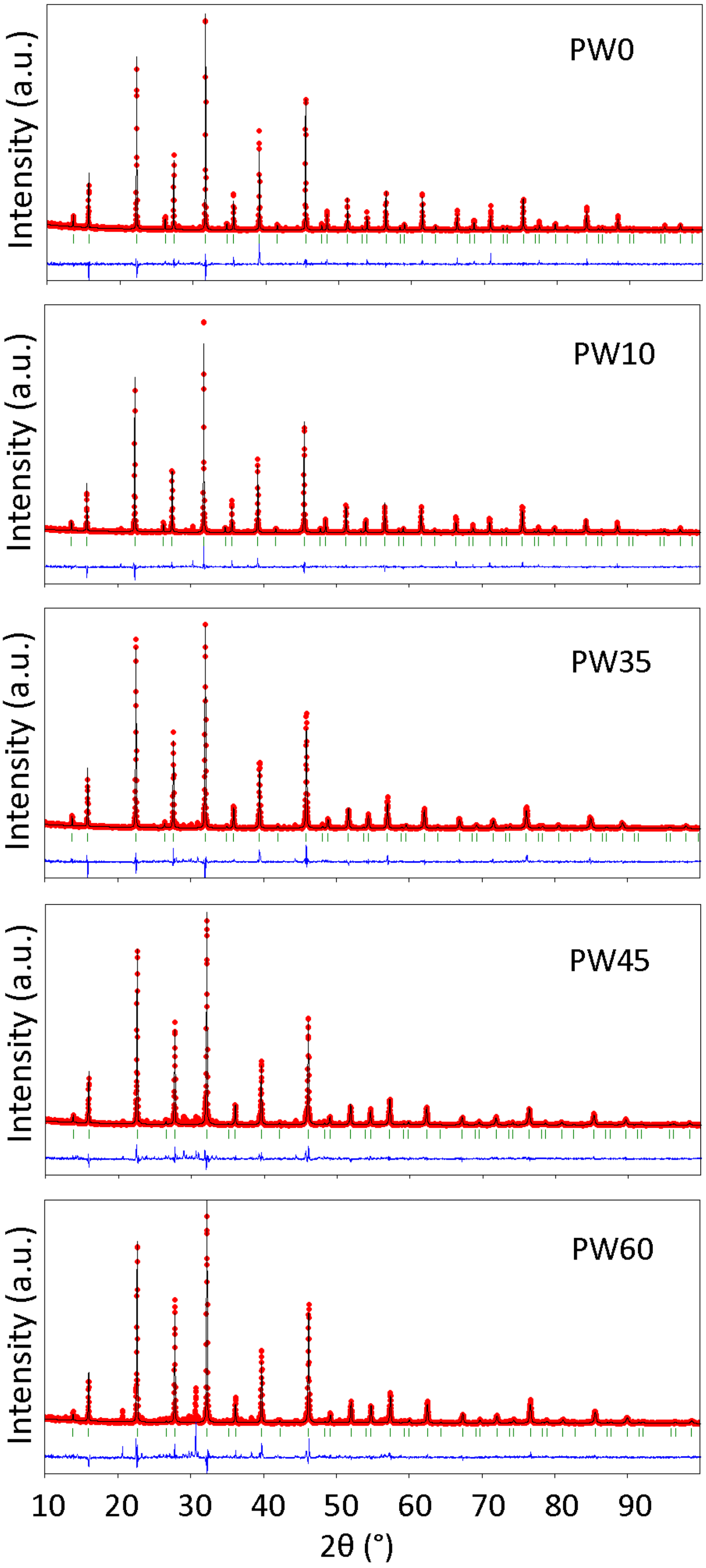
Intensity (a.u.)
PW0
Intensity (a.u.)
PW10
Intensity (a.u.)
PW35
Intensity (a.u.)
PW45
Intensity (a.u.)
PW60
10
20
30
40
50
60
70
80
90
2θ (°)

Figure S2 X-ray diffraction patterns with Rietveld refinement for the Cs$_2$AgIn$_x$Bi$_{1-x}$Br$_6$ double perovskite polycrystalline powders for the different indium percentages. The percentages of indium in the plots refers to the amount of indium in the starting precursors. The red dots represent the experimental points, while the black pattern is the calculated one. The green vertical lines represent the peaks positions, and the blue line shows the residuals.

Table ST3 Lattice parameters and atomic coordinates from Rietveld refinements of the XRD patterns of Cs2AgBi1-xInxBr6 polycrystalline samples. Number in parentheses are statistical errors of the last significant digit. In $Fm\bar{3}m$, the atoms are located at the following Wyckoff positions Cs: 8c(1/4,1/4,1/4) , Bi/In: 4a(0,0,0) , Ag: 4b(1/2,1/2,1/2) , Br: 24e(x,0,0).

x	a (Å)	x(Br)	Occ(In)	R_p/R_{wp}
0	11.27245(16)	0.25154(54)	-	16.6/22.1
10	11.25002(14)	0.2510(4)	0.031(10)	14.0/17.9
35	11.1789(3)	0.2487(4)	0.404(12)	13.3/17.7
45	11.1450(3)	0.2473(6)	0.542(15)	13.8/19.6
60	11.1184(4)	0.2456(8)	0.678(18)	15.0/20.1

Table ST4 Indium percentage in powders extrapolated by inductively coupled plasma mass spectroscopy (ICP-MS) and XRD, in comparison with the starting percentage of indium in the precursors powders.

%In precursors	%In (ICP-MS)	%In (XRD)
0	0.0120 ± 0.0325	0
10	10.1 ± 0.2	0.31 ± 0.1
40	35.9 ± 0.5	40.4 ± 1.2
50	45.2 ± 0.5	53 ± 1.5
60	59.3 ± 0.9	70 ± 1.8

1.3 Thin films

X-ray diffraction on the thin films (quartz) has been measured using PANalytical X'Pert PRO Diffractometer with Cu-Kα radiation, as in the case of powders. In Figure S3 we show the patterns for all the samples. We measured the thickness of the perovskite films using a DektakXT Stylus profiler, and the results are reported in Table ST5. The thickness decreases with increasing percentage of indium because the solubility of the starting solution decreases when indium is added, so the molarity was slightly different for each sample.

Table ST5 Thicknesses of each thin film of $Cs_2AgIn_xBi_{1-x}Br_6$ for each indium percentage.

Thin film	Thickness (nm)
TF0	142 ± 10
TF10	167 ± 10
TF35	180 ± 10
TF45	200 ± 10
TF60	280 ± 10

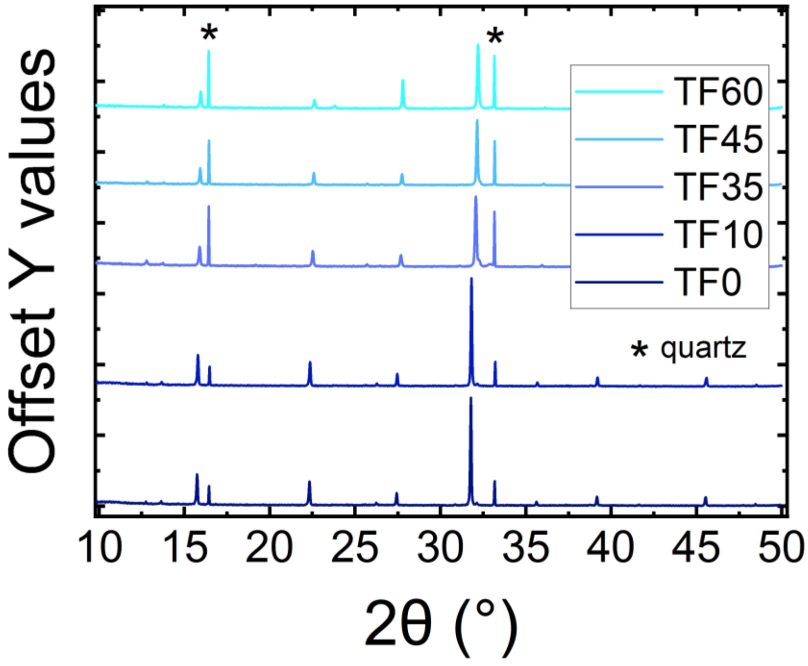

Figure S3 X-ray diffraction pattern for the $Cs_2AgIn_xBi_{1-x}Br_6$ thin films for the different indium percentages. The asterisks indicate the quartz peaks.

2) Structural transition

Temperature-dependent X-ray diffraction and heat capacity measurements have been used on the powders to investigate the presence of a low-temperature structural transition in the alloyed materials, as it appears in the neat $Cs_2AgBiBr_6$ double perovskite [2]. Sample cooling was achieved employing an Oxford Cryosystems PheniX cryostat. The heat capacity has been measured with the use of a Quantum Design Physical Properties Measurement System, varying the temperature of the samples.

The $(400)_c$ peak of the room-temperature cubic phase was measured on the powder samples as a function of temperature. Figure S4a) and S5a) show the peak splitting for PWD10 and PWD35 relative to the cubic-to-tetragonal transition, while the lattice parameters determined from the fits are reported in panels S4b) and S5b). The absence of a clear anomaly at the transition in panel c) of Figure S6 can be explained considering the transition of the neat $Cs_2AgBiBr_6$ to be close to a tricritical point [3], as explained in the main text.

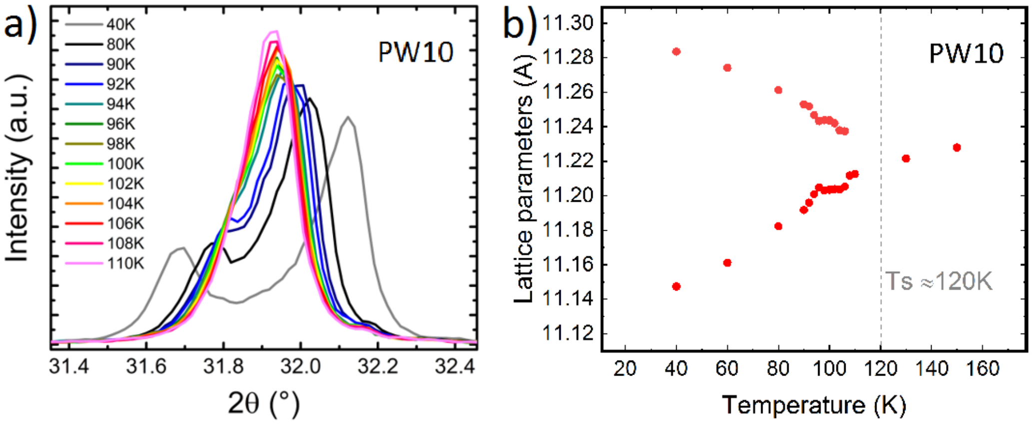

Figure S4 a) X-ray diffraction pattern of PWD10 plotted in the range ~ [31.3-32.5] °, where the (400)c peak of the cubic room-temperature structure is present, in function of temperature. b) Lattice parameters extrapolated from the peaks fitting in function of temperature.

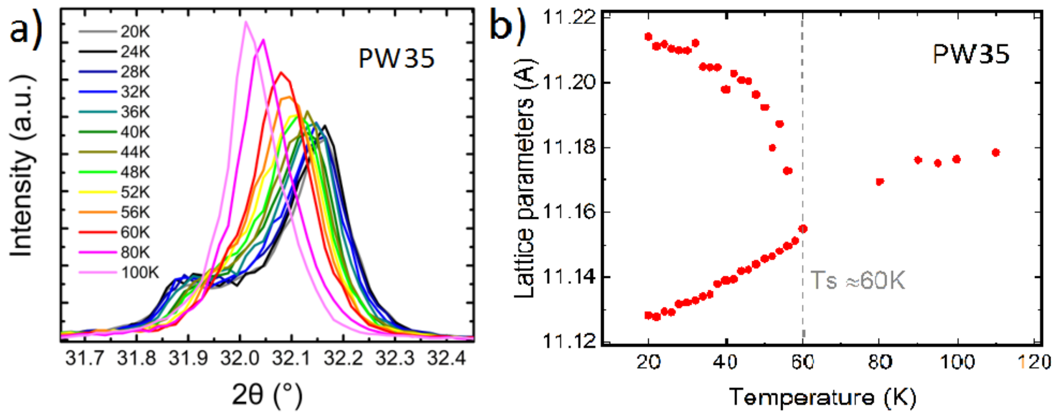

Figure S5 a) X-ray diffraction pattern of PWD35 plotted in the range ~ [31.3-32.5] °, where the (400)c peak of the cubic room-temperature structure is present, in function of temperature. b) Lattice parameters extrapolated from the peaks fitting in function of temperature.

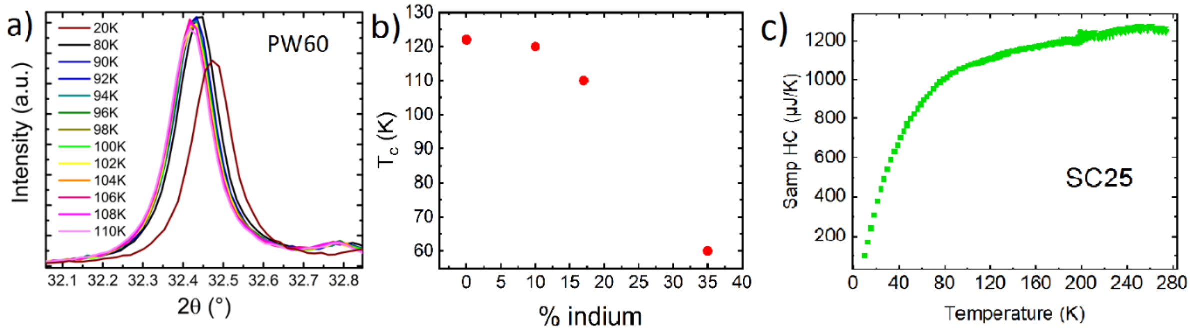

Figure S6 a) X-ray diffraction pattern of PWD60 plotted in the range ~ [31.3-32.5] °, where the (400)c peak of the cubic room-temperature structure is present, in function of temperature. b) Transition temperature T_c in function of indium concentrations. Values are also taken from heat capacity measurements. c) heat capacity measured on the single crystal SC25.

3) Photoluminescence, Ellipsometry and pictures

Steady-state photoluminescence has been measured by exciting single crystals and polycrystalline powders of $Cs_2AgIn_xBi_{1-x}Br_6$ with a fibre-coupled 405nm laser. The signal has been detected from the top surface via a fibre bundle (Ocean Optics QR600-7-SR125BX) coupled with a spectrometer (QE Pro, Ocean Optics). Figure S7a) shows the PL emission from polycrystalline powders samples. The photoluminescence peak position shifts towards higher energies with increasing indium concentration, as we can also notice in the measurements on single crystals in panel b.

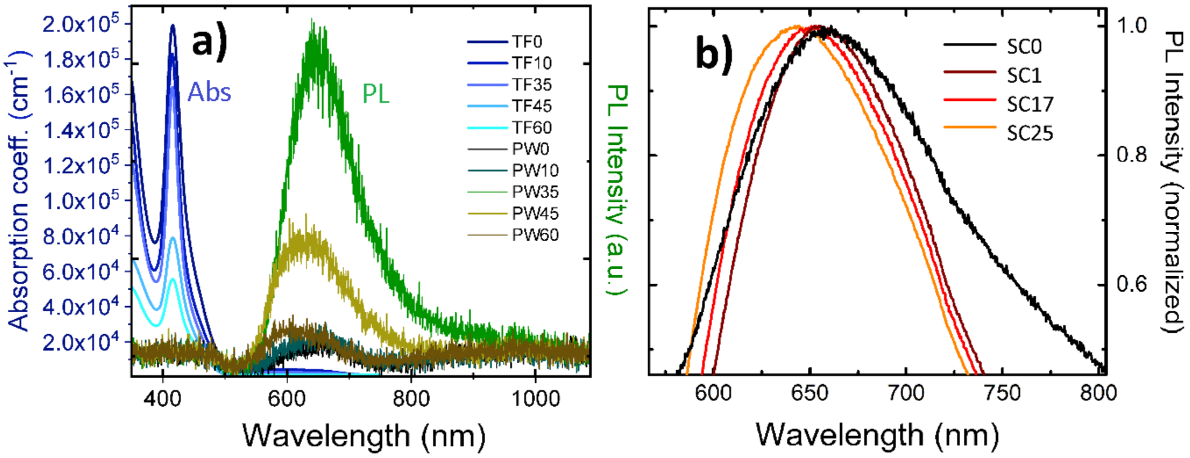

Figure S7 a) Absorption measured on thin films and photoluminescence emission measured on polycrystalline powders samples. b) Normalized photoluminescence spectrum of $Cs_2AgIn_xBi_{1-x}Br_6$ single crystal samples, excited with a 405 nm laser.

We show pictures of thin films, single crystals and polycrystalline powder samples in Figure S8 below. The maximum crystal size is about 2mm.

The n and k values derived from spectroscopic ellipsometry data are shown in Figure S9. The measurements were carried out using a J.A.Woollam RC2 ellipsometer. Due to the small size of the crystals, the maximum angle at which the data (from 210-1690 nm) could be measured off the surface of the crystals was 65° (along with 55°) using focussing lens. Cubic spline fits to the data were carried out for the refractive indices and surface roughness of the crystals, which ranged from 3-8 nm. The fitting was performed in CompleteEase software (J.A.Woollam company). The mean squared error of the fits ranged from 2.3 (for SC1) to 13.1 (for SC25).

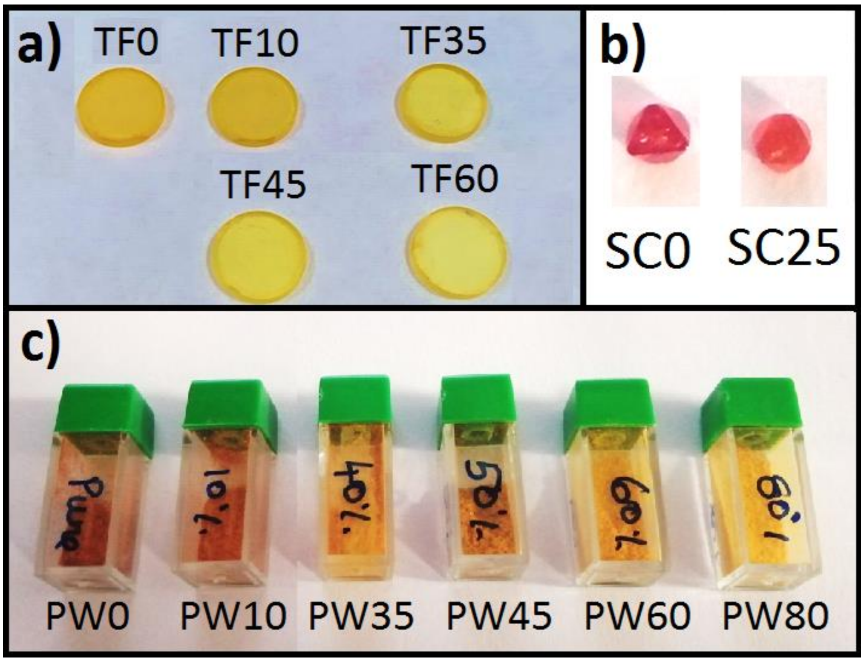

Figure S8 Pictures of $Cs_2AgIn_xBi_{1-x}Br_6$ a) thin films, b) single crystals and c) polycrystalline powders.

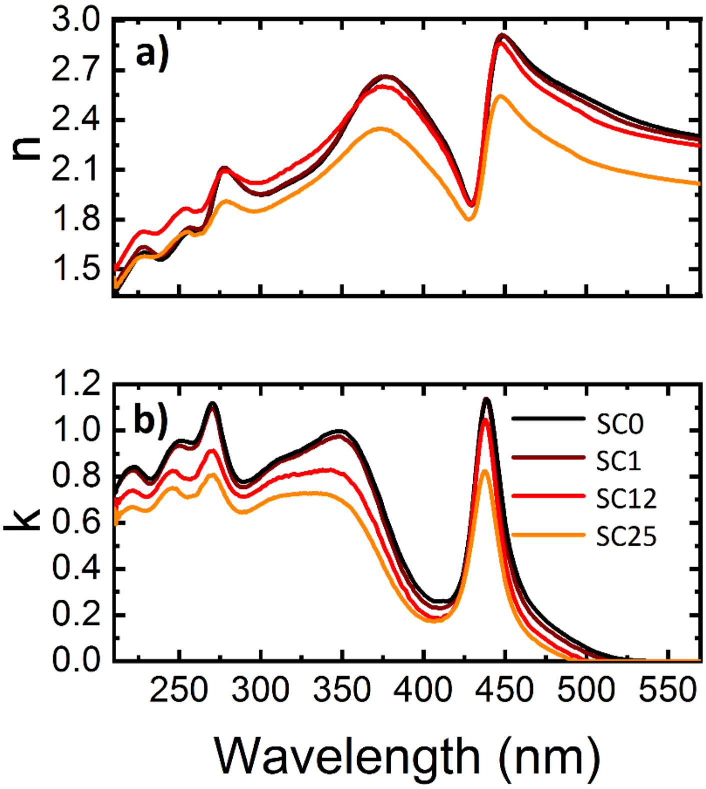

Figure S9 Optical constants a) n and b) k determined from spectroscopic ellipsometry measurements of single crystals with a range of indium contents.

4) Computational methods

We modelled the alloys of $Cs_2AgIn_xBi_{1-x})Br_6$ employing a 2x2x2 supercell of the primitive Fm-3m lattice of $A_2BB'X_6$ double perovskite. For the different indium concentrations (i.e. x = 0.125, 0.25, 0.5) we replace 1,2 and 4 bismuth atoms with indium, respectively, as shown in Figure S10.

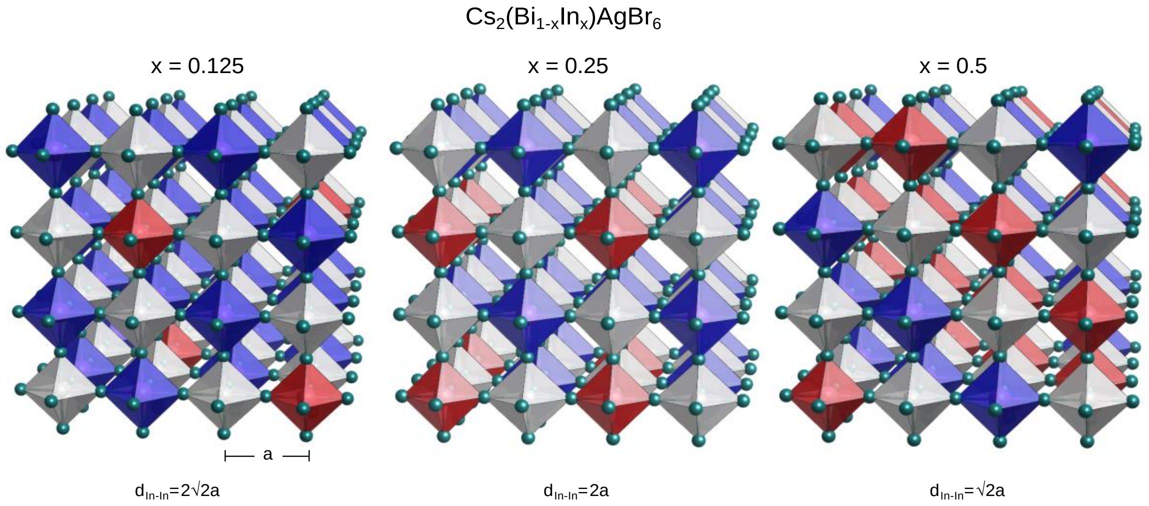

Figure S10 Representation of the simulated supercell of the primitive Fm-3m for the $Cs_2AgIn_xBi_{1-x}Br_6$ structure.

The lattice parameters are kept fixed at the measured values of 11.27 Å, 11.21 Å, 11.18 Å and 11.15 Å for x=0, 0.125, 0.25 and 0.5, respectively, and we perform only an optimization of the atomic positions, within DFT-PBE.

All the structural optimization calculations are based on the density-functional theory as implemented in the Quantum-Espresso Suite [4]. We used fully-relativistic norm-conserving pseudopotentials [5], the PBE exchange correlation functional [6] from pseudo-dojo [7]. The kinetic energy for the plane waves cut-off was set at 100 Ry, and for the supercells we employed a 2x2x2 Γ-centered k-point grid. Spin-orbit coupling was taken into account for all electronic structure calculations, including hybrid calculations.

The spectral functions representing the band structures of all doped systems were obtained by the zone unfolding technique [8,9], as implemented for plane waves in the Quantum espresso package [9]. The procedure consists of calculating the electron spectral function in the Lehman representation given by:

$$\mathrm{A}_{\mathbf{k}}(\varepsilon) = \sum_{\mathrm{m}\mathbf{K}} P_{\mathrm{m}\mathbf{K},\mathbf{k}} \delta(\varepsilon - \varepsilon_{\mathrm{m}\mathbf{K}}), \qquad (1)$$

where $\varepsilon_{\mathrm{m}\mathbf{K}}$ is the energy of the Kohn-Sham state $|\Psi_{m\boldsymbol{K}}^{d}\rangle$ in the doped structure, and $P_{\mathrm{m}\mathbf{K},\mathbf{k}}$ is the spectral weight given by:

$$P_{\mathrm{m}\mathbf{K},\mathbf{k}} = \sum_{n} |\langle\psi_{m\boldsymbol{K}}^{d}|\psi_{nk}\rangle|^2. \quad (2)$$

The spectral weight represents the overlap probability between the state $|\psi_{m\boldsymbol{K}}^{d}\rangle$ of wavevector **K** with all Kohn-Sham states $|\psi_{nk}\rangle$in the conventional cell of wavevector **k**. In practice, we evaluate $P_{\mathrm{m}\mathbf{K},\mathbf{k}}$ using an equivalent expression to Eq. (2) that requires only the plane wave coefficients of the states in the doped structure [8,9]. We select a set of 200 K-points that are mapped one by one onto equally-spaced k-points along the L-Γ-X path in the BZ of the conventional cell. The mapping is performed via a reciprocal lattice vector of the doped structure. For each of these K-points we calculate $P_{\mathrm{m}\mathbf{K},\mathbf{k}}$ and $\varepsilon_{\mathrm{m}\mathbf{K}}$, in order to evaluate the spectral function $\mathrm{A}_{\mathbf{k}}(\varepsilon)$. This quantity represents essentially the momentum-resolved density of states of the electrons in the doped structure.

For the HSE [11] hybrid functional calculations we employed the VASP code [12], within the projector augmented wave method [13], and including spin-orbit coupling effects. We set the cut-off for the kinetic energy of the wavefunctions at 400 eV, and perform calculations employing the Γ-point and checked convergence with a 2x2x2 Γ-centered k-point grid.

For the calculations on the unit-cell shown in Figure 3b of the main text, we employ a dense Γ-centered 30x30x30 k-point mesh and an adaptive smearing of 25-100 meV. For calculations employing the 2x2x2 super-cell shown in Figure 3d, a Γ-centered 6x6x6 uniform k-point mesh was employed for the sampling of the Brillouin zone and an adaptive gaussian smearing of 100-150 meV. We used the HSE hybrid functional to calculate the band-gap correction of the doped systems and rigidly shifted the spectra in Figure 3c.

5) PDS and Tauc-plot

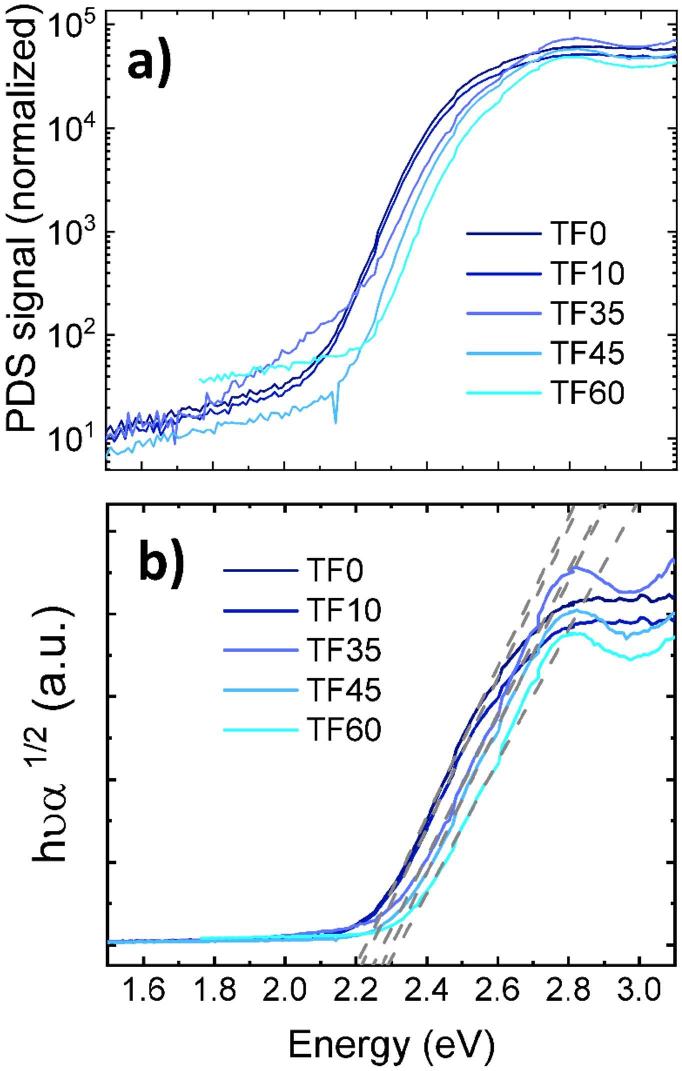

Figure S11 a) PDS absorption measurements on thin films and b) tauc-plots measured on $Cs_2AgBi_{1-x}In_xBr_6$ for different concentrations of indium.

Photothermal Deflection Spectroscopy (PDS) is a scatter-free surface sensitive absorption measurement capable of measuring several orders of magnitude weaker absorbance than the band edge absorption. For the measurements, a monochromatic pump light beam is shined on the sample (double-perovskite thin film on quartz substrate), which on absorption produces a thermal gradient near the sample surface via non-radiative relaxation induced heating. This results in a refractive index gradient in the area surrounding the sample surface. This refractive index gradient is further enhanced by immersing the sample in an inert liquid FC-72 Fluorinert® (3M Company) which has a high refractive index change per unit change in temperature. A fixed wavelength CW laser probe beam is passed through this refractive index gradient producing a deflection proportional to the absorbed light at that particular wavelength, which is detected by a photo-diode and lock-in amplifier combination. Scanning through different wavelengths provide the complete absorption spectra. The perovskite samples were deposited on quartz substrates for PDS measurements following the same deposition method described in the main manuscript. We show the normalized PDS signal in panel a of Figure S11, and the Tauc plot in panel b.

In Table ST6 we show the values of the band gap extrapolated from the Tauc-plot and also values of the Urbach energy, extrapolated from the exponential fitting of the absorption curve with a linear subtracted background (Figure S12).

Table ST6 Values of the band gaps and Urbach energies (Eu) for $Cs_2AgIn_xBi_{1-x}Br_6$ thin films.

Thin film	Band gap (eV)	E_u (meV)
TF0	2.23	65.13 ± 0.77
TF10	2.24	63.22 ± 0.89
TF35	2.27	61.91 ± 0.55
TF45	2.30	54.03 ± 0.67
TF60	2.32	50.91 ± 0.76

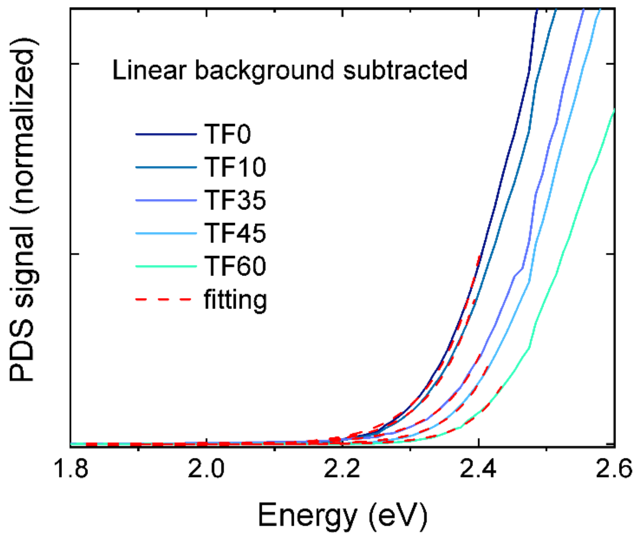

Figure S12 PDS signal with a linear background subtracted, from measurements on thin films of $Cs_2AgBi_{1-x}In_xBr_6$with different percentages of indium, and fitting.

6) Device characterization

6.1 Preparation

Devices were fabricated in the n-i-p structure: ITO/SnO_2 nanoparticles/$Cs_2AgBi_{1-x}In_xBr_6$/Spiro-OMeTAD/Ag. Pre-cut ITO coated glasses were cleaned by sequential sonication in soap, water, acetone and isopropanol. After being dried with a N_2 gun, the substrates were further cleaned with O_2 plasma for 10 minutes. Tin oxide nanoparticles were prepared using 0.178 mL SnO_2 dispersion (15% in H_2O) in 0.822 mL of milliQ water. For the perovskite $Cs_2AgBi_{1-x}In_xBr_6$ layer we dissolved the precursors: AgBr (99%), BiBr3 (>98%), InBr3 (99.998%) and CsBr (99.9%) in DMSO (0.3M). The solution has been spin-coated at 4000 rpm (with an acceleration of 4000 rpm/s) for one minute in air and then heated at 285°C for 5 minutes. The hole transport material (Spiro-OMeTAD, Lumtec) was dissolved in chlorobenzene (85 mg/mL) and doped with 20 µl of LiTFSI (500 mg/ml in BuOH) and 30 µl of tert-butylpyridine. The solution was then deposited on the active layer by spincoating in air at 2000 rpm (2000 rpm/sec) for 45 sec. The devices were then left overnight in a desiccator in air atmosphere, and then completed by the evaporation of 100 nm silver contacts. All the characterizations were performed in air.

6.2 Characterization

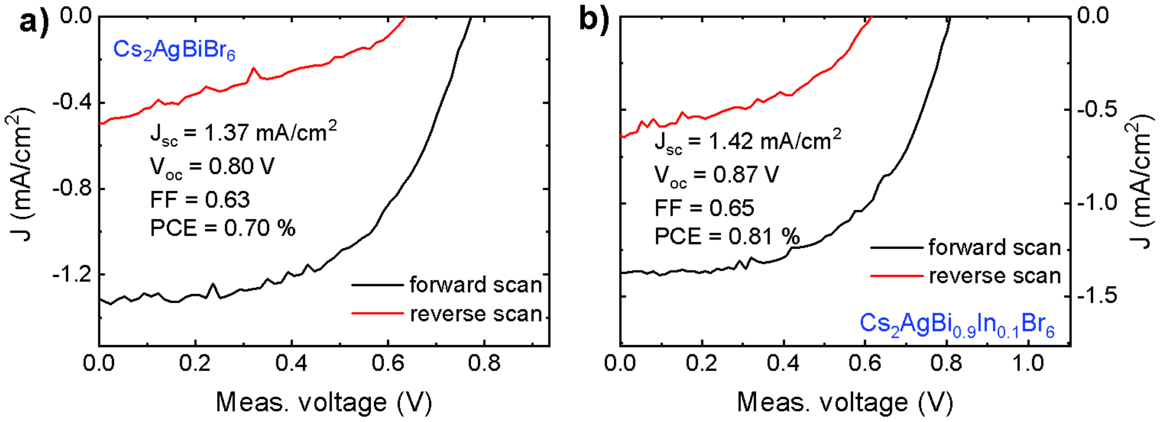

Figure S13 J-V scans for the best devices made with a) $Cs_2AgBiBr_6$ and b) $Cs_2AgBi_{0.9}In_{0.1}Br_6$ as absorbing layer.

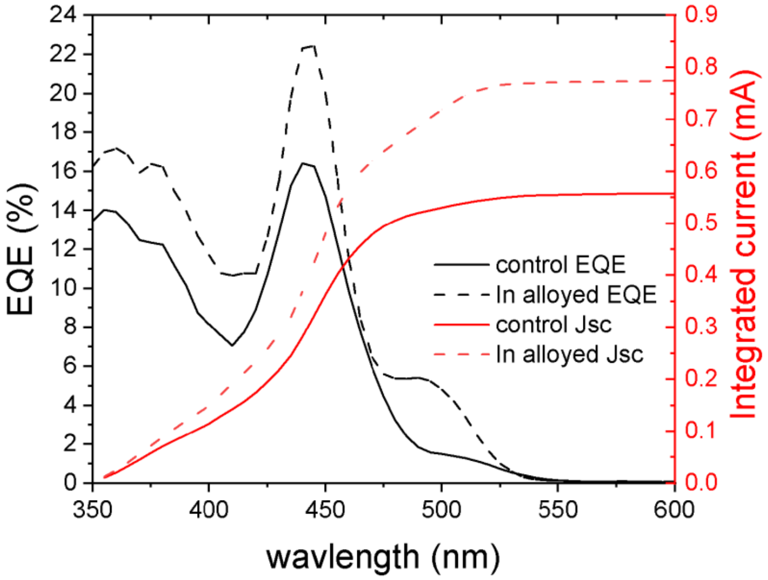

Figure S14 External Quantum Efficiency (EQE) and Integrated current measured on devices with (dotted lines) and without (continuous lines) indium.

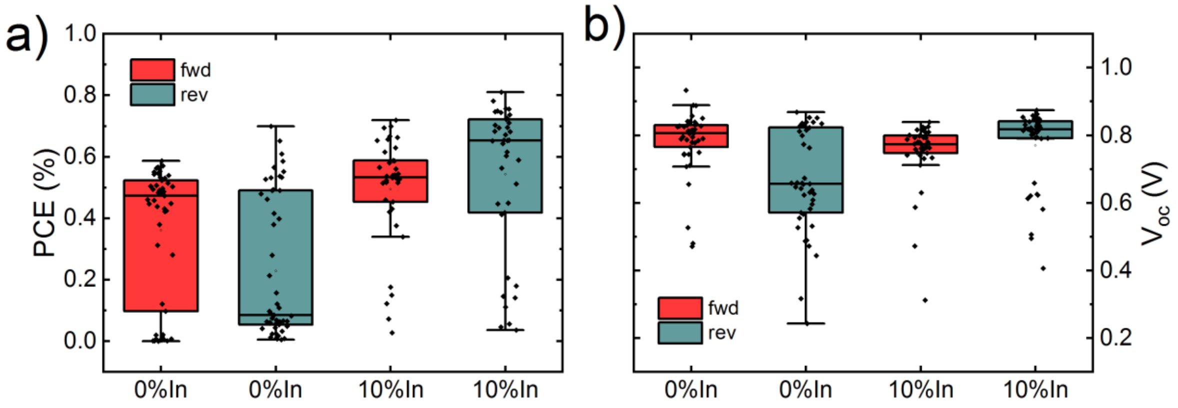

Figure S15 a) Power conversion efficiency (PCE) and b) open-circuit voltage (V_{oc}) for devices with and without indium, for the forward and reverse scans.

[1] Rodríguez-Carvajal, J. Recent Advances in Magnetic Structure Determination by Neutron Powder Diffraction. *Phys. B (Amsterdam, Neth.)* **1993**, 192, 55−69.

[2] Schade, L.; Wright, A. D.; Johnson, R. D.; Dollmann, M.; Wenger, B.; Nayak, P. K.; Prabhakaran, D.; Herz, L. M.; Nicholas, R.; Snaith, H. J.; Radaelli, P. G. Structural and Optical Properties of $Cs_2AgBiBr_6$ Double Perovskite. *ACS Energy Lett.* **2019**, *4* (1), 299– 305.

[3] Salje, E. K. H. Physical Properties and Thermodynamic Behaviour of Minerals. *NATO ASI Series* Serie C: Mathematical and Physical Sciences Vol 225, 84-85, 108-109, **1987.**

[4] Gianozzi, P.; Andreussi, O.; Bumme, T.; Bunau, O.; Nardelli, M. B.; Calandra, M.; Car, R.; Cavazzoni, C.; Ceresoli, D. and Cococcioni, M. *J.Phys.:Condens.Matter* **2017** 29, 465901.

[5] Hamann, D. R. Optimized Norm-Conserving Vanderbilt Pseudopotentials *Phys. Rev. B* **2013** 88, 085117.

[6] Perdew, J. P. and Ernzerhof, M. Rationale for mixing exact exchange with density functional approximations *J. Chem. Phys*. **105** (22): 9982–9985.

[7] van Setten, M. J.; Giantomassi, M.; Bousquet, E.; Verstraete, M. J.; Hamann, D. R.; Gonze, X., and Rignanese, G.-M. The Pseudodojo: Training and Grading a 85 Element Optimized Norm-Conserving Pseudopotential Table. *Computer Physics Communications* **2018** 226, 39-54.

[8] Popescu, V. and Zunger, A. Extracting E Versus k Effective Band Structure from Supercell Calculations on Alloys and Impurities. *Phys. Rev. B* **2012** 85, 085201.

[9] Medeiros, P. V. C.; Stafström, S. and Björk, J. Effects of Extrinsic and Intrinsic Perturbations on the Electronic Structure of Graphene: Retaining an Effective Primitive Cell Band Structure by Band Unfolding. *Phys. Rev. B* **2014** 89, 041407.

[10] Zacharias, M. and Giustino, F. Theory of the Special Displacement Method for Electronic Structure Calculations at Finite Temperature. *Phys. Rev. Research* **2020**, 2, 013357

[11] Heyd, J. Hybrid Functionals Based On a Screened Coulomb Potential. *J. Chem. Phys.* **2003** 118 (18), 8207.

[12] Kresse, G. and Furthmüller, J. Efficient Iterative Schemes for *ab initio* Total-Energy Calculations Using a Plane-Wave Basis Set. *Phys. Rev.* **1996**, 54, 11169.

[13] Blöchl, P. E. Projector Augmented-Wave Method. *Phys. Rev. B* **1994** 50, 17953.